



HAL
open science

An investigation of structural, thermal, and electrical conductivity study for understanding transport mechanisms of CuWO_4 and $\alpha\text{-CuMoO}_4$ compounds

N. Chakchouk, Karim Karoui, N. Drissi, F. Jomni, A. Ben Rhaiem

► **To cite this version:**

N. Chakchouk, Karim Karoui, N. Drissi, F. Jomni, A. Ben Rhaiem. An investigation of structural, thermal, and electrical conductivity study for understanding transport mechanisms of CuWO_4 and $\alpha\text{-CuMoO}_4$ compounds. RSC Advances, In press, 14 (1), pp.46-58. hal-04596624

HAL Id: hal-04596624

<https://univ-tours.hal.science/hal-04596624>

Submitted on 9 Jun 2024

HAL is a multi-disciplinary open access archive for the deposit and dissemination of scientific research documents, whether they are published or not. The documents may come from teaching and research institutions in France or abroad, or from public or private research centers.

L'archive ouverte pluridisciplinaire **HAL**, est destinée au dépôt et à la diffusion de documents scientifiques de niveau recherche, publiés ou non, émanant des établissements d'enseignement et de recherche français ou étrangers, des laboratoires publics ou privés.

Investigation of structural, thermal, and electrical conductivity study for understanding transport mechanisms of CuWO_4 and $\alpha\text{-CuMoO}_4$ compounds

N. CHAKCHOUK^a, K. KAROUI^{a,c,*}, N. DRISSI^b, F. JOMNI^d, A. BEN RHAJEM^a

a- University of Sfax, Laboratory of Spectroscopic Characterization and Optics of Materials, Faculty of Sciences, B.P. 1171, 3000, Sfax, Tunisia.

b- Department of physics, Faculty of Science, King Khalid University, P.O. Box 9004, Abha 61413, Saudi Arabia

c- GREMAN UMR 7347-CNRS, CEA, INSACVL, University of Tours, Blois, France

d- Université de Tunis El Manar, Laboratoire LMOP, LR99ES17, El Manar, 2092 Tunis, Tunisia

*Corresponding author: E-mail: karouikarim36@yahoo.com

Tel: 0021625648756

Abstract

Recently, inorganic oxide components with high ionic conductivity have been widely explored. Due to their high stability, safety, and energy density properties. In this context, the present work focuses on the inorganic oxides CuMO_4 ($M=W, \text{Mo}$), which have been successfully synthesized using the traditional solid-state method. They were characterized by X-ray powder diffraction, thermal analysis, and complex impedance spectroscopy. X-ray diffraction data refined via the Rietveld method indicated that these compounds are well crystallized in the triclinic system with $P\bar{1}$ space group. Besides, the electrical conductivity behavior of these materials was analyzed using the impedance spectroscopy technique in the frequency ranges of 10^0 to 10^6 Hz and in the temperature ranges of 443 K to 563 K. The absence of a phase transition observed in the calorimetric study was confirmed by the σ_g and ω_h variations as a function of temperature. The AC conductivity was analyzed by Jonscher's power law. The outcomes of the study on charge transportation in CuMO_4 (where $M=W, \text{Mo}$) suggest that the overlapping large polaron tunneling (OLPT) mechanism was present in CuMoO_4 , while the correlated barrier hopping (CBH) and the non-overlapping small polaron tunneling (NSPT) were present in CuWO_4 . A correlation between the crystal structure and the ionic conductivity was established and discussed. For two titled compounds, modulus analysis revealed that the charge carriers were mobile over short and long distances at low and high frequencies, respectively. The temperature variation of the M'' peak showed a thermally activated relaxation process.

Keywords : *Crystal structure, Thermal analysis, Electrical conductivity, Conduction mechanism, Modulus analysis.*

1.Introduction

During the past decade, interest in the relationship between crystal structures and physical properties has experienced a revival with the discovery of high-temperature superconductivity and its severe dependence on details of the crystal structure. There are various typical structure types for binary oxides with the general formula AMO_4 , in which A and M cations can be multivalently and compositely replaced.

Many AMO_4 oxides, such as arsenates, chromates, silicates, vanadates, and phosphates, are isostructural with zircon ($I4_1/a$ m d, No. 141, $Z=4$); a few AMO_4 oxides, such as periodates, germinates, tungstates, and molybdates, crystallize in the scheelite structure ($I4_1/a$, No. 88, $Z=4$); a large number of tantalates, molybdates, and tungstates crystallize with the wolframite structure ($P2/c$, No. 13, $Z=2$); relatively few AMO_4 oxides exist as M' -fergusonite structures ($P2_1/c$, No. 14, $Z=2$) or M' -fergusonite under normal conditions, but lots of AMO_4 oxides transform from zircon or scheelite structures to M' -fergusonite and M' -fergusonite under pressure.

Among these, the wolframite structure AMO_4 (where A denotes transition metal ions, and M denotes divalent cations) is particularly notable. Copper oxides ($CuMO_4$, With $M=W, Mo$) are an important inorganic materials that have gained enormous scientific importance due to their wide-ranged applicability, including optical fibers, scintillator materials, industrial catalysts, microwave applications, humidity sensors, photoluminescence, and due to their magnetic, electric, and electrochemical properties [1-7]. Among molybdates, the $CuMoO_4$ compound is a very complex polymorphism [8–11]. To date, six different polymorphs of $CuMoO_4$ have been identified in the literature: namely ambient condition α - $CuMoO_4$ (green phase) [8], high-temperature β - $CuMoO_4$ [9], low-temperature γ - $CuMoO_4$ (brownish red phase) [10], high pressure (HP) $CuMoO_4$ -II [11], distorted wolframite $CuMoO_4$ -III [12] and monoclinic ε - $CuMoO_4$ [13]. Both compounds, $CoMoO_4$ -II and $CuMoO_4$ -III, are isostructural to the tungstates $CoWO_4$ and $CuWO_4$, respectively [14].

Additionally, copper tungstate ($CuWO_4$) is regarded as a superior material for creating the positive electrodes of rechargeable Li batteries [15] and for synthesizing W-Cu pseudo alloys with a copper content of 10-35 mol% that are almost porous-free [15].

However, there are still a lot of unanswered questions regarding the physical properties of ($CuMO_4$, with $M=W, Mo$).

A comprehensive examination of the literature revealed that there are no records of electrical properties studies on (α -CuMoO₄) and (CuWO₄). In order to link these characteristics to the structural aspects of these materials, we consequently decided to record electrical and dielectric properties as a function of frequency and temperature. Additionally, this study might provide important information about the conduction process and the electrical conductivity of the material.

2. Experimental methods

2. 1. Synthesis procedure

In a standard process, polycrystalline CuMO₄ (M = W, Mo) powder samples were synthesized via the conventional solid-state reaction by mixing high-purity precursors of CuO (Sigma–Aldrich, $\geq 99\%$), MoO₃ (Sigma–Aldrich, $\geq 99\%$), WO₃ (Sigma–Aldrich, $\geq 99\%$).

In the first step, the starting precursors were mixed in stoichiometric quantities and initially meticulously ground in an agate mortar, sealed in platinum crucibles, and then heated at 773 K for 16 h. After heat treatment, the samples have been grinded and then reheated again between 923 K and 1023 K to ensure homogeneity, as summarized in **Table 1**. Afterward, the reaction products were cooled at a rate of 393 K h⁻¹ to room temperature.

Finally, the colors of these synthetic samples, which vary depending on the metal used, are in accordance with those revealed in the literature, as suggested in **Table 1**.

Note that the following stages are sequentially reached with an increasing sintering temperature: a formation of isthmuses between grains, a compaction of grains, and finally, their growth.

The crystallization and purity of these phases were checked out by X-ray diffraction (XRD) on the powder. Then, based on the Rietveld method, the data collected at room temperature were analyzed by the Fullprof software. Differential scanning calorimetric analysis was carried out using a DSC (Q-100) TA instrument with a scanning rate of 10°C/min between 283 K and 483 K temperature range. To carry out electrical measurements, the powder resulting from the grinding was shaped as a pellet (8 mm in diameter and 1.1 mm in thickness) in a uniaxial hydraulic press at a pressure of 3 tons/cm². The measurements were performed using a 1260 Solartron Impedance Analyzer under vacuum operating in the temperature range of 443 K to 563 K.

3. Results and discussion

3. 1. Crystalline parameters

The purity of the synthesized compounds and their crystalline characteristics were obtained through an XRD pattern registered at room temperature. **Figure. 1(a, b)** illustrates the experimental and calculated XRD profiles of the compounds α -CuMoO₄ and CuWO₄, respectively, as well as the corresponding discrepancies. The full pattern refinement was analyzed by the Rietveld method using the Fullprof program. The lattice parameters and the $P\bar{1}$ space group reported in the bibliographic data were used as a starting point [8, 16]. All Bragg peaks were successfully indexed and satisfactorily modeled. The quality factors that show good agreement between the experimental (red dots) and calculated (black solid line) profiles are $\chi=4.02$ and $\chi=3.1$ of the compounds α -CuMoO₄ and CuWO₄, respectively. Indeed, we can notice the presence of a small extra peak identified by an asterisk in the X-ray powder pattern (**Figure. 1a**) of α -CuMoO₄, indicating the presence of a secondary phase of MoO₃ in the vicinity of 2%, which crystallizes in the orthorhombic system [17]. The unit cell parameters of MoO₃ are mentioned by Nora Wooster (2015).

The estimation results of the structural parameter are illustrated in **Table 2**. These results are in good agreement with literature [8, 16]. This study demonstrated that the system and crystal structure could be changed by switching the divalent cation (from W⁺ to Mo⁺).

3. 2. Structural description

The structure of CuWO₄ is implied in **Figure. 2a**. In this structure, the copper atom is surrounded by six oxygen atoms, four of which are approximately square planar configuration and the remaining two at a longer distance, completing an elongated octahedron. The tungsten atom is located within a slightly distorted octahedron but is considerably displaced from its center.

The WO₆ and CuO₆ octahedra are connected by a corner, and the CuO₆ octahedra exhibit an elongated pseudo-tetragonal geometry due to the Jahn-Teller effect of the Cu²⁺ cation [16, 18]. It is clear from the figure that although CuWO₄ is triclinic, its structure is topologically related to that of monoclinic wolframite (P2/c). The W-O distances of the WO₆ octahedra are slightly distorted, similar to those of wolframite, and range from 1.79 Å - 2.20Å.

Nevertheless, the monoclinic P2/c symmetry is lowered to the triclinic $P\bar{1}$ symmetry due to the Cu²⁺ Jahn-Teller effect, which decreases the degeneracy of 3D orbitals [18].

As a result, the CuO₆ octahedra adopt an elongated pseudo-tetragonal geometry with two axial Cu-O distances near 2.50 Å and four planar Cu-O distances at 1.93 Å.

Additionally, the alternating CuO_6 and WO_6 octahedra form endless zigzag chains by sharing the edges of copper and tungsten atoms in the CuWO_4 sequence of layers that are located between the oxygen sheets. In contrast, as illustrated in **Figure. 2 b**, the $\alpha\text{-CuMoO}_4$ structure can be characterized by MoO_4 tetrahedra, CuO_5 square pyramidal polyhedra, and CuO_6 distorted octahedra that are joined by common corners and edges to create layers. For octahedrally coordinated CuO_6 , the average Cu-O distances in $\alpha\text{-CuMoO}_4$ range from 1.94 Å to 2.53 Å, but for pyramidal CuO_5 (C_{4v}) they vary from 1.90 Å to 2.53 Å. While the Mo-O bond distances range from 1.74 Å to 2.38 Å.

It is important to note that the symmetry elements and the relative positions of the atoms distinguish the difference between the structures of CuWO_4 and $\alpha\text{-CuMoO}_4$. This appears to be caused, most probably, by the potent Jahn-Teller effect present in CuO_6 octahedra, which causes a significant elongation. Also, the geometry of the MO_6 ($M=\text{W}, \text{Mo}$) and CuO_6 octahedra and their connection have a significant impact on the band gap as well as the associated optical, electrical, and magnetic properties.

3. 3. Thermal analysis

Differential scanning calorimetric is typically used to examine the thermal transformation of a material, such as crystallization, transition to glass, melting, etc. To prevent the material from reacting with the atmosphere, this analysis was carried out under a supply of an inert gas (nitrogen). The results of the thermal analysis (DSC) for CuMO_4 ($M = \text{W}, \text{Mo}$) samples in the heating temperature range of 283 K to 483 K and with a ramp rate of $10^\circ\text{C} / \text{min}$, are displayed in **Figure. 3**. We notice that this study shows that no exothermic or endothermic peaks are displayed in the temperature range studied, which can be attributed to the absence of structural transitions in the two compounds.

3. 4. Electrical properties

3. 4. 1. Nyquist diagram and equivalent circuit

After the structural and thermal analysis, the electrical characteristics of the compounds were carried out by complex impedance spectroscopy (CIS) which operates over wide ranges of temperature and frequency. It provides information on the microstructure of various materials, including the electrode interfaces, grains, and grain boundaries. This versatile technique gives information on the mobility of individual components within the system and the occurrence of specific interactions. It displays a direct connection between the response of the real system and the ideal circuit made by the electrical components. Through this method, a specimen undergoes

a low sinusoidal perturbation. The impedance is evaluated by analyzing the current response to the varying frequency of the imposed alternating voltage over a wide range, and subsequently, it is separated into real and imaginary components.

Indeed, the complex impedance Z^* is divided into its real part Z' and its imaginary part Z'' :

$$Z^* = Z'(w) - jZ''(w) \quad (1)$$

Figures 4 (a, b) and 5 (a, b) depict the Cole–Cole plot of the typical complex impedance plane for CuMO_4 ($M = \text{W, Mo}$) samples at a temperature interval ranging from 443 K to 563K. It is worth noting that the centers of the depressed semicircles are located below the real axis, indicating that both materials exhibit non-Debye behavior [19].

For the Mo-based compound, the experimental data showed the existence of two semi-circles, each placed within a different frequency domain, indicating the presence of two contributions. The high-frequencies semicircle is attributed to the grain effect and the other at low frequencies is attributed to the effect of grain boundary [20]. On the other hand, to visualize these two contributions (grains and grain boundary elements), we performed a deconvolution of the Nyquist curve recorded at **T = 563 K (Fig. 6)**.

In actuality, we can distinguish between the two contributions by looking at the resistance value provided by the adjustment; the arc with the lowest resistance value is attributed to the effect of the grain, whereas the other is attributed to the grain boundary effect. The higher resistivity of the grain boundary is reflected in the increased arc dispersion at low frequencies. Based on the ZView software [21], the $-Z'' = f(Z')$ plots were adjusted by an equivalent electrical circuit formed by a resistance (R_g) parallel with the fractal capacitance (CPE_g) describing the response of the grains in series with a resistance (R_{gb}) parallel to the capacitance (C_{gb}) describing the grain boundary (**inset of Fig. 4**).

Whereas, for the W-based compound, these spectra are composed of a single semi-circular arc at each temperature suggesting the dominance of the grain contribution.

The spectra were adequately modeled by a single-cell circuit model, formed by a resistance (R_g) in parallel with the series combination (C_g and CPE_g) as depicted in the **inset of Fig. 5**.

In this model, R_g introduces the resistance, C_g represents the capacitance and CPE_g is the non-ideal capacitor usually known as the constant phase element.

Furthermore, we observe that according to **Figures 4 and 5**, the radii of the semicircles decrease with increasing temperature in the Cole–Cole plot, suggesting that the conduction mechanism is thermally activated. The latter is known as the negative temperature coefficient of resistance (NTCR), which is a characteristic of semiconductor compounds [22].

Indeed, it is important to note that the non-ideal Debye behavior and the observed depression of the semicircles are both explained by the presence of a constant phase element (CPE) in these equivalent circuit models [23].

The impedance of the CPE contribution is an empirical function of the following type:

$$Z_{cpe} = \frac{1}{Q*(j\omega)^\alpha} \quad (2)$$

Where Q is the capacitance value of the CPE element, ω is the angular frequency; and α is a parameter indicating the change of the compressed semicircle from an ideal semicircle.

The frequency behavior of the complex impedance parts ($-Z''$) of the α -CuMoO₄ and CuWO₄ samples, for distinct temperatures, is displayed in **Figure.7 (a, b)** and **Figure.8 (a, b)** respectively.

The spectra explicitly describe the strength and the position of the relaxation peak which is found to be different for several sintering temperatures. We can observe that the impedance plots are characterized by the presence of maximum peaks (Z''_{max}) at a specific frequency known as the relaxation frequency, f_{max} . The relaxation peak shifts to very high frequencies as the temperature rises. These findings demonstrate the presence of the electrical relaxation phenomenon, characterize its nature, and highlight its strength in our material [24, 25]. As temperatures increase, a significant broadening of the asymmetric peaks is observed, indicating a temperature-dependent relaxation process in the system that lengthens the relaxation period (depicted by the increased width of the peaks). This may be explained by the fact that the relaxation process is caused by defects or vacancies at high temperatures, while immobile species or electrons are accountable at low temperatures [26, 27].

Additionally, the height of the relaxation peaks is also impacted in addition to peak broadening. As the temperature rises, the height of the relaxation peaks declines, suggesting a loss of resistive characteristics. It also suggests the existence of a relaxing process that is initiated by heat and implies that the relaxation mechanism is thermally stimulated.

Finally, for all temperatures and for higher frequencies, the imaginary part of $-Z''$ is merged, which may probably indicate an accumulation of space charges in the system. There was also a perfect superposition between the experimental scatter data and the theoretical line for these curves.

The advantageous justification for the choice of the equivalent circuit retained is verified by the variations of the experimental values of (Z') and ($-Z''$) according to those calculated using the parameters of the equivalent circuit model at different temperatures (**Figure. 9 (a, b)**, **Figure. 10 (a, b)**). It is clear from these graphs that the slope produced by a linear fitting of the data

points at all temperatures is almost equal to the unit. This behavior leads us to the conclusion that the chosen equivalent circuit accurately describes the electric characteristics of the samples and that there is a good correlation between the theoretical (calculated line) and experimental data (scatter) of the real and imaginary impedance parts.

3. 5. Conductivity studies

3. 5. 1. DC conductivity

The conduction process in amorphous semiconductors involves temperature-dependent Dc conductivity. Electrical conductivity is a thermally activated process that relies on the ordered movement of lightly bound charged particles while being affected by a continuous electric field. The following equation can be used to determine the electrical conductivity of the grain (σ_g) at each temperature, derived from the resistance values obtained from the equivalent circuit [28]:

$$\sigma_g = \frac{e}{R_g S} \quad (3)$$

Where R_g is the resistance of grain determined by the adjustment, S is the area of the electrode that is deposited on the pellet, and e is the thickness of the sample.

Figure. 11 (a, b) displays the conductivity (σ_g) of the α -CuMoO₄ and CuWO₄ samples in a temperature range of 443 K to 563 K, at a constant voltage of 1.5 V. These curves clearly demonstrate that the response of $\ln(\sigma_g T)$ versus $1000/T$ represents a straight line or a continuity of curve slope, indicating the absence of phase transition in these samples over the temperature range studied, which was verified by the DSC diagram (**Figure. 3**).

Indeed, as can be seen from the graph, the Dc conductivity rises linearly over the entire temperature range as a result of an increase in the number of charge carriers that are made available by the increase in thermal energy. This is due to thermally assisted tunneling of charge carriers in the band tail of the localized [29], which leads to the Arrhenius equation:

$$\sigma_g T = A \exp\left(\frac{-E_{a,g}}{K_B T}\right) \quad (4)$$

Where K is the Boltzmann constant, A is the pre-exponential factor which includes the mobility of the charge carrier and the density of states, T is the absolute temperature, and $E_{a,g}$ is the activation energy for the conductivity of grain. The values of the activation energies obtained from the linear fit of the data points, are $E_{a,g}=0.73$ eV for CuWO₄, and $E_{a,g}=0.60$ eV for α -CuMoO₄.

Table 3 presents a comparison between the electrical properties of CuWO₄ and α -CuMoO₄. The table shows that α -CuMoO₄ has a higher conductivity due to its lower activation energy

$E_{a,g}$. The influence of structural features on the conductivity and activation energy of each phase can be deduced from these data. For the α -CuMoO₄ compound, the highest conductivities and the lowest $E_{a,g}$ are correlated with the better mobility of the Mo cation in the corresponding frameworks. In fact, the greater Mo-O bond distances (1.74 Å - 2.38 Å) compared to those of W-O (1.79 Å - 2.20 Å) result in a weakening of the attraction between Mo⁺ and O₂ and a release of ion attachment to the crystal, which lowers the potential barrier and requires lower activation energy, thereby increasing conductivity. In addition, it is also associated with the dimension of the tunnels in α -CuMoO₄.

On the other hand, it appears that the conductivity of α -CuMoO₄ is slightly higher than that of the CuWO₄ compound, which is due to the smaller mass and ionic radius of molybdenum ($m_{Mo}=1.59310^{-22}$ g, $r_{Mo^+}=0.59$ Å) compared to the tungsten ($m_W=3.052 \cdot 10^{-22}$ g, $r_{W^+}=0.60$ Å) and consequently it is more mobile than W⁺.

Additionally, the large value of the pre-exponential factor, which is proportional to the density of the charge carriers and the disorder within the material, can also be used to explain the increase in conductivity of the compound of α -CuMoO₄.

Indeed, the pre-exponential factor obtained thanks to the Arrhenius parameterization law, is given by [30]:

$$A_0 = \left(e^2 \times a^2_h \times \frac{v_0}{6 K_B} \right) \times N(T) \times \exp\left(\frac{S_\mu}{K_B}\right) \quad (5)$$

Where a_h is the jump distance, v_0 is the natural frequency of vibration, $N(T)$ is the number of charge carriers and S_μ is the migration entropy.

3. 5. 2. AC electrical conductivity

The nature of defect centers in disordered systems has been extensively studied using AC conductivity measurements, which should account for this type of conduction. In most polar semiconductor oxides, the high-frequency dependence of the AC conductivity is often observed in experimental settings. This observation can then be explained in terms of thermally stimulated charge carrier hopping between sites localized above the potential barrier. In fact, an empirical formula is used to determine the conductivity values of the material (σ_{ac}):

$$\sigma_{ac}(\omega) = \frac{e}{S} \times \frac{Z'}{Z'^2 + Z''^2} \quad (6)$$

Where e/S is the geometric report of the pellet, Z' and Z'' are the real and the imaginary parts of the complex impedance data.

The variation of the AC conductivity of CuMO₄ (M= Mo, W) samples at different temperatures is shown in **Figure. 12 (a, b)**. These spectra are described by two regions and are theoretically analyzed using Jonscher's universal power law [31, 32].

$$\sigma_{ac}(\omega) = \sigma_{dc} + A\omega^s \quad (7)$$

With σ_{dc} represents the value of the conductivity of direct current at low frequency; A is a parameter dependent on temperature that determines the strength of polarizability, and s is the power law exponent that reflects the extent to which the charge carriers interact with the lattice of CuMO₄ (M = W, Mo) and varying between the range of 0 to 1. For ideal Debye-type behavior, the parameter s=1, $A\omega^s$ is the ac conductivity encompassing all dispersion phenomena.

As evident from the conductivity plots, two distinct regions can be observed at low and high frequencies. In the low-frequency range, the conductivity spectra exhibit nearly constant values, indicating that the charge transport can be described by a hopping model, as defined by the first term of the Jonscher equation. Ions successfully hop from one site to an adjacent vacancy in this area, causing long-range transitional motion of the ions, which contributes to the direct conductivity.

In contrast, the second part of the equation can be used to determine the asymptotic form of the conductivity, often referred to as the dispersive regime, at high frequencies.

This dispersion could be connected to the anticipated behavior of space charges, given that their influence diminishes with increasing temperatures and frequencies [33]. The proposed spectra demonstrate that this is not always the case, since there are curves for where the increase is not observed, indicating the presence of space charges even at high frequencies.

In addition, we observed that the AC conductivity rises in tandem with temperature. Given that electrical conduction in the ceramic system is a thermally stimulated process, this indicates that a greater number of free charge carriers are generated at high temperatures, which promotes enhanced conductivity and suggest the properties of the semiconductor [34].

In fact, equation (6) can be mentioned by the Almond–West relation [35]:

$$\sigma_{ac}(\omega) = \sigma_{dc} \left(1 + \left(\frac{\omega}{\omega_h} \right) \right) \quad (8)$$

With ω_h , the frequency corresponding to the onset appearance of the dispersion region is known as the hopping frequency of the charge carrier. An increase in temperature, the ω_h shifts to a higher frequency range, indicating that the hopping frequency is thermally stimulated. It is stated in the following way:

$$\omega_h = \left(\frac{\sigma_{dc}}{A}\right)^{1/s} \quad (9)$$

Figures. 13 (a) and (b) reveal the plot of $\text{Ln}(\omega_h)$ as a function of $(1000/T)$ relative to the conduction of grain for $\alpha\text{-CuMoO}_4$ and CuWO_4 compounds, respectively. It represents the continuity of the curve slope, referring to the absence of a phase transition within these samples at the studied temperature range. This was confirmed by the DSC (Differential Scanning Calorimetric) diagram.

These evolving processes exhibit an Arrhenius-like behavior with activation energies, determined from a straight-line adjustment of the data points, roughly equal to $E_{a,g}=1.36$ eV for Mo-based compound and $E_{a,g}= 0.56$ eV for W-based compound. In fact, these results differ from those found recently on the DC conductivity of grains (σ_g), demonstrating that the mobility of charge carriers in the studied compounds is not insured by a straightforward hopping mechanism [36].

A suggested approach to understand the charge transfer mechanism in CuMO_4 ($M = \text{W, Mo}$) can be constructed by considering several theoretical models based on the behavior of s (T) with temperatures.

According to the literature, various models have been proposed, such as the non-overlapping small polaron tunneling (NSPT) model put forth by Long [37], the overlapping large polaron tunneling (OLPT) model proposed by Long [38], the quantum mechanical tunneling (QMT) model put forth by Austin-Mott [39], and the correlated barrier hopping (CBH) model, as introduced by Elliot [40, 41]. These diverse conduction models are based on two distinct processes: the quantum mechanical tunneling effect and the classical hopping of charge carriers across a barrier, or a combination of the two. Additionally, various hypotheses have been made about the atoms or electrons (or polarons) accountable for serving as carriers.

In this context, the variations of the exponent (s) with temperature in our systems are illustrated in **Figure. 14 (a, b)**.

In the temperature range of 443 K to 533 K, the parameter (s) for CuWO_4 shows an increase with temperature, indicating the presence of a correlated barrier hopping (CBH) mechanism. However, within the temperature range of 548 K to 563 K, the exponent (s) displays a tendency to decrease with rising temperatures. Therefore, this result suggests that the non-overlapping small polaron tunneling (NSPT) model is a suitable mechanism to characterize electrical conduction. For $\alpha\text{-CuMoO}_4$, the asymptotic patterns of ' s ' decrease with increasing temperature, establishing a minimum at 473 K, then it starts to increase with rising temperature.

Therefore, the OLPT model appears to be the most suitable model for characterizing the electrical conduction mechanism in the studied compound.

3. 6. Complex modulus analysis

The electrical relaxation characteristics occurring in materials are frequently justified using the electrical modulus formalism [42]. The electrode polarization and the relaxation frequency of conductivity are displayed by electrical modulus analyses. This formalization provides a more comprehensive understanding of charge transport processes, including conductivity relaxation, ion dynamics as a function of temperature and frequency, and the electrical transport mechanism. This formalism is complementary to the conductivity study.

In fact, the dielectric modulus (M^*) is defined as:

$$M^* = M' + j M''$$

$$= M_\infty \left[1 - \int_0^\infty e^{-i\omega t} \left(-\frac{d\varphi(t)}{dt} dt \right) \right] \quad (10)$$

Where $M' = \omega C_0 Z''$ and $M'' = \omega C_0 Z'$ are respectively the real and imaginary parts of the modulus, C_0 is the geometrical capacitance defined as $C_0 = \epsilon_0 S/e$ (where ϵ_0 denotes the permittivity of free space, S represents the area of the electrode, and e signifies the thickness). Additionally, $\varphi(t)$ represents the function that shows the time evolution of the electric field within the materials.

Figure.15 (a, b) shows the variation of the imaginary part of the modulus (M''), as a function of frequency for the two titled compounds in the measured temperature range (443 K- 563 K).

For the Mo-based compound, this graph displays two asymmetric relaxation peaks for each temperature. The influence of the grain boundary is demonstrated by the tiny peak observed at low frequencies. Whereas, the second peak found at high frequencies is connected to the relaxation process of grains. In contrast, for the W-based compound, these plots show the appearance of a single peak in the modulus spectra, confirming the single relaxation phenomenon of the material studied. These results are in good agreement with those of the Nyquist plots.

Furthermore, it is evident that the illustrations of these figures reveal that the charge carriers are mobile over long distances in the frequency range below the maximum peak

M''_{\max} . The area above is where charge carriers are spatially connected to potential wells and are only capable of localized motion within these wells while maintaining their mobility over short distances.

Additionally, the presence of these peaks in the modulus spectra explains the conductivity relaxation processes. With rising temperatures, the relaxation peak moves up to a higher frequency spectrum. The relaxation process is thus temperature-dependent and it assigns a correlation between the movements of the mobile ions as the temperature increases.

In fact, the charge carriers become more accelerated and thermally active. This results in a decrease in the relaxation time, an increase in the relaxation frequency, and a shift in the frequency of the relaxation peaks [43]. This behavior assumes that the jumps of the charge carrier are taken into account and that the relaxation depends on the temperature.

Added to this, at lower frequencies, the values of the imaginary parts of M'' approach zero, showing that the electrode effect can be neglected in the modulus representation.

On the other hand, the temperature dependency of the characteristic relaxation frequency f_p is plotted in **Figure.16 (a, b)**. It is clear that the relaxation frequency satisfies the Arrhenius law given by the following equation:

$$f_p = f_0 \exp\left(\frac{-E_a}{k_B T}\right) \quad (11)$$

Where f_0 is the pre-exponential factor, E_a is the activation energy for the relaxation frequency and k_B denotes the Boltzmann constant. The activation energy calculated by a linear fit to the data points is $E_a = 1.28$ eV for a Mo-based compound and $E_a = 0.56$ eV for a W-based compound.

The activation energies derived from $\ln(\sigma_g T) = f(1000/T)$ and $(\ln f_p) = f(1000/T)$ for the two title compounds are grouped in **Table 4**. It can be seen that the values of the activation energies obtained from the relaxation frequency and those obtained from the conductivity are different for the α -CuMoO₄ sample. This means that there is a partial blocking of the movements of the charge carriers by the grain boundaries [44]. However, the latter has a significant impact on the total conductivity values of the material.

Contrarily, in the case of the compound based on tungsten, the activation energy estimated from the relaxation frequency is very close to that obtained from conductivity. This observation demonstrates that the total conductivity is equal to the grain conductivity rather than being influenced by the grain boundaries. This proves that conduction and relaxation are ensured by the same mechanism in the material.

Conclusions

Briefly, our study examined the impact of replacing tungsten ($r_{W^{+}} = 0.60\text{\AA}$) with molybdenum ($r_{Mo^{+}} = 0.59\text{\AA}$) on both structural and electrical properties. Initially, we prepared powders of $CuMoO_4$ and $CuWO_4$ using a solid-state reaction method. The XRD diffractograms demonstrate that both $CuMoO_4$ and $CuWO_4$ crystallize in the triclinic system with the same space group $P\bar{1}$. From a structural standpoint, it is important to note that the replacement of tungsten with molybdenum results in a significant change in the lattice parameters, volume, the distances between W and Mo, and angles. Thermal analysis indicates the absence of any exothermic or endothermic peaks within the temperature range of 283 K to 483 K, which can be attributed to the absence of structural transitions in the two titled compounds.

An equivalent circuit for the electrochemical cell with both compounds has been proposed.

Furthermore, the study of dc conductivity implies that Mo^{+} conduction is preferable to W^{+} conduction as a result of its small mass and small ionic size. Additionally, it has been discovered that at various temperatures, the ac conductivity spectra response follows the Jonscher's power law. The variations of the exponent 's' as a function of temperature confirm that the charge transport mechanisms are the non-overlapping small polaron tunneling (NSPT) model, the correlated barrier hopping (CBH) model for the sample of $CuWO_4$ and the OLPT approach for α - $CuMoO_4$. Eventually, the temperature variation of M'' peak showed a thermally activated relaxation process.

Conflicts of interest

There are no conflicts to declare.

Acknowledgment

The authors extend their appreciation to the Deanship of Scientific Research at King Khalid University for funding this work through small group Research Project under grand number RGP.1/41/44.

References

1. W. Xiusheng, F. Chao, C. Jufang, G. Chunye, L. Wei, Effect of W doping on phase transition behavior and dielectric relaxation of CuMoO_4 obtained by a modified sol-gel method, *Mat. Res. Express.*, 7 (2020) 016309.
2. K. Seevakan, Structural, morphological and magneto-optical properties of CuMoO_4 , electrochemical nanocatalyst as supercapacitor electrode *Ceram, Int.*, 44 (2018) 20075–20083.
3. G. Steiner, R. Salzer, W. Reichelt, Temperature dependence of the optical properties of CuMoO_4 *Fresenius, J. Anal. Chem.*, 370 (2001) 731–734.
4. N. Joseph, Glass-free CuMoO_4 ceramic with excellent dielectric and thermal properties for ultralow temperature cofired ceramic applications *ACS Sustain, Chem. Eng.*, 4 (2016) 5632–5639.
5. M. Naja, A. Abbasi, M. M. Farahani, V. H Rodrigues, Synthesis, characterization and crystal structure of a copper molybdate coordination polymer as an epoxidation catalyst, *Inorg. Chim. Acta.*, 433(2015) 21–25.
6. D. Dongwei, R. Lan, X. Wei, Beanland Richard, W. Huanting, T. Shanwen, Preparation of a hybrid $\text{Cu}_2\text{O}/\text{CuMoO}_4$ nanosheetelectrode for high-performance asymmetric supercapacitors, *J. Mat. Chem A.*, 4 (2016) 17749-17756.
7. H. Ehrenberg, H. Weitzel, J. Garcia-Jaca, F. Rodriguez, D. Hernandez, Optical study of the piezochromic transition in CuMoO_4 by pressure spectroscopy, *Phy.Rev.B.*, 61(2000) 16497.
8. M. Benchikhi, Characterization and photoluminescence properties of ultrafine copper molybdate($\alpha\text{-CuMoO}_4$) powders prepared via a combustion-like process *Int, J. Min. Met. Mater.*, 23 (2016)1340–1345.
9. R. Kohlmuller, J. P. Faurie, Etude des systemes $\text{MoO}_3\text{-Ag}_2\text{MoO}_4$ et $\text{MoO}_3\text{-MO}$ (MCu, Zn, Cd), *Bull. Soc. Chim. Fr.*, 11 (1968) 4379–4382.
10. H. Ehrenberg, H. Weitzel, H. Paulus, M. Wiesmann, G. Wltschek, M. Geselle, H. Fuess, Crystal structure and magnetic properties of CuMoO_4 at low temperature (β -phase), *J. Phys. Chem. Sol.*, 58 (1997)153–160.
11. A. W. Sleight, High Pressure CuMoO_4 . *Mater. Res. Bull.* 8 (1973) 863–866.
12. R. Tali, V. V. Tabachenko, L. M. Kovba, L. N. Dem Öyanets, Kristallicheskaya struktura CuMoO_4 , *Zhurnal. Neorg. Khimii.*, 36 (1991) 1642–1644.
13. J. Baek, A. S. Sefat, D. Mandrus, P. S. Halasyamani, A New Magnetically Ordered Polymorph of CuMoO_4 : Synthesis and Characterization of $\epsilon\text{-CuMoO}_4$, *Chem. Mater.*, 20 (2008) 3785–3787.

14. H. Ehrenberg, M. Wiesmann, J. Garcia-Jaca, H. Weitzel, H. Fuess, Magnetic structures of the high-pressure modifications of CoMoO_4 and CuMoO_4 , *J. Mag. Magn Mate.*, 182 (1998) 152-160.
15. O. Yu. Khyzhun, V. L. Bekenev, Yu. M. Solonin, First-principles calculations and X-ray spectroscopy studies of the electronic structure of CuWO_4 , *J. Alloys. Comp.*, 480 (2009) 184–189.
16. J. Ruiz-Fuertes, D. Errandonea, A. Segura, F.J. Manjón, Zh. Zhu and C.Y. Tu, Growth, characterization, and high-pressure optical studies of CuWO_4 , *High. Pres. Resea.*, 28 (2008) 565–570.
17. N. Wooster, The crystal structure of Molybdenum Trioxide, MoO_3 , *Zeitschrift für Kristallographie, Cryst. Mater*, 18 (2015) 504-5012
18. J. B. Forsyth, C. Wilkinson, A. I. Zvyagin, The antiferromagnetic structure of copper tungstate, CuWO_4 , *J. Phys.: Condens. Matter.*, 3 (1991) 8433-8440.
19. M. Mumtaz, M. Naveed, B. Amin, M. Imran and M. N. Khan, Temperature dependent impedance spectroscopy of $(\text{Co}_3\text{O}_4)_x/\text{CuTi-1223}$ nanoparticles-superconductor composites, *Ceram. Int.*, 44 (2018) 4351–4359.
20. K. Karoui, A. B. Rhaïem, F. Jemni, $\text{Li}_2\text{M}(\text{WO}_4)_2$ ($\text{M} = \text{Ni}, \text{Cu}, \text{Co}$): electrical, thermal, and optical properties, *Ionics.*, 27 (2021) 1511–1524.
21. D. Johnson, ZPlot, ZView Electrochemical Impedance Software, Version 2.3b (Scribner Associates, Inc., North Carolina, 2000).
22. I. Dakhlaoui, K. Karoui, F. Hajlaoui, M. Zaghrioui, N. Audebrand, M. Dallone and F. Jomni, A new supramolecular semiconductor palladium (II) complex $[(\text{CH}_3)_3\text{N}(\text{CH}_2)_3\text{Br}]_2\text{Pd}_2\text{Cl}_6$: structural study, optical and electrical properties, *New J. Chem.* 47 (2023) 8042-8049.
23. N. Chakchouk, K. Ben Brahim, M. Ben Gzaïel, A. Oueslati, Investigation of optical and electrical properties of the semiconducting α - KZnPO_4 compound, *RSC Adv.*, 12 (2022) 6831-6840.
24. S. Kour, H. Mahajan, R. Mukherjee, Influence of sintering temperature on impedance and modulus spectroscopy of nickel-substituted cobalt ferrite, *J Mater Sci: Mater Electron.*, 34 (2023) 594-608.
25. M. M. Rahman, N. Hasan, M.A. Hoque, M.B. Hossen, M. Arifuzzaman, *Results Phys.*, 38 (2022) 105610.
26. B. N. Parida, R. D. Piyush, R. Padhee, R. N. P. Choudhary, Synthesis and characterization of a tungsten bronze ferroelectric oxide, *Adv. Mat. Lett.* 3 (2012) 231–238.

27. L. Singh, L. Dhavala, R. Bhimireddi, A. A. Ansari, S. Kumar, V. Srivastava f, R. N. Rai, Q. V. Le, Y. Lee, Low-cost flame synthesized $\text{La}_{2/3}\text{Cu}_3\text{Ti}_4\text{O}_{12}$ electro-ceramic and extensive investigation on electrical, impedance, modulus, and optical properties, *Cer. Inter.*, 49 (2023) 21795-21803.
28. K. Karoui, A. Mahmoud, A. Ben Rhaiem, F. Boschini, Electrical and electrochemical properties of $\text{Li}_2\text{M}(\text{WO}_4)_2$ (M = Ni, Co and Cu) compounds, *RSC. Adv.*, 9 (2019) 6785-6792.
29. M. Ganaie, S. Ahmad, S. Islam, M. Zulfeqar; Dc, Ac Conductivity and Dielectric Analysis of SeTe Alloy, *Advan. Science. Letters.*, 20 (2014) 1360-1363.
30. B. Louati, F. Hlel, K. Guidara, *J. Alloy Comp.*, 486 (2009) 299-303.
31. A. K. Jonscher, *Dielectric relaxation in solids* (Chelsea Dielectric Press, London, 1983), p. 380.
32. R. Ltaoui, A. Triki, S. Hcini, A. Oueslati, S. Zemni, O. Kanoun, Conduction mechanisms and complex impedance analysis in $\text{La}_{0.6}\text{Sr}_{0.4}\text{FeO}_3$ ceramic, *J. Electro.*, 50 (2023) 121–138.
33. A. Q. Abdullah, Optical and structural investigation of synthesized PVA/Pb Snanocomposites, *Chem. Mater. Res.*, 26 (2015) 6939-6944.
34. R. N. Bhowmik, G. Vijayasri, *J. appl. phys.*, 114 (2013) 223701-223708.
35. H. Nefzi, F. Sediri, H. Hamzaoui, N. Gharbi, *Mater. Rese. Bulletin.*, 48 (2013) 1978-1983.
36. N. Chakchouk, B. Louati, K. Guidara, Electrical properties and conduction mechanism study by OLPT model of NaZnPO_4 compound, *Mater. Rese. Bulletin.*, 99 (2018) 52–60.
37. M. Dult, R.S. Kundu, S. Murugavel, R. Punia, N. Kishore, *Phys. B.*, 452 (2014) 102–107.
38. A. R. Long, Frequency-dependent loss in amorphous semiconductors, *Adv. Phys.*, 31 (1982) 553-637.
39. I. G. Austin, N. F. Mott, *Polarons in crystalline and non-crystalline materials.*, *Adv. Phys.*, 18 (1969) 41–102.
40. S. R. Elliot, *Adv. Phys.*, 36 (1987) 135–217.
41. M. Krimi, K. Karoui, J. J. Suñol, A. B. Rhaiem, Phase transition, impedance spectroscopy and conduction mechanism of $\text{Li}_{0.5}\text{Na}_{1.5}\text{WO}_4$ material, *Physica E: Low-dimensional, Syste. Nanos.*, 102 (2018) 37-145.
42. C. T. Moynihan, L. P. Boesch, N. L. Laberge, Decay function for the electric field relaxation in vitreous ionic conductors, *J. Phys. Chem. Glasses.*, 14122 (1973) 122-125.
43. V. Thakur, A. Singh, R. Punia, S. Dahiya, L. Singh, *J. Alloys. Comp.*, 696 (2017) 529–537.
44. C. H. Hervoche, M. C. Steil, R. Muccillo, Synthesis by the polymeric precursor technique of $\text{Bi}_2\text{Co}_0.1\text{V}_0.9\text{O}_5.35$ and electrical properties dependence on the crystallite size, *J. Sol. Stat Scie*, 6 (2004) 173-177.

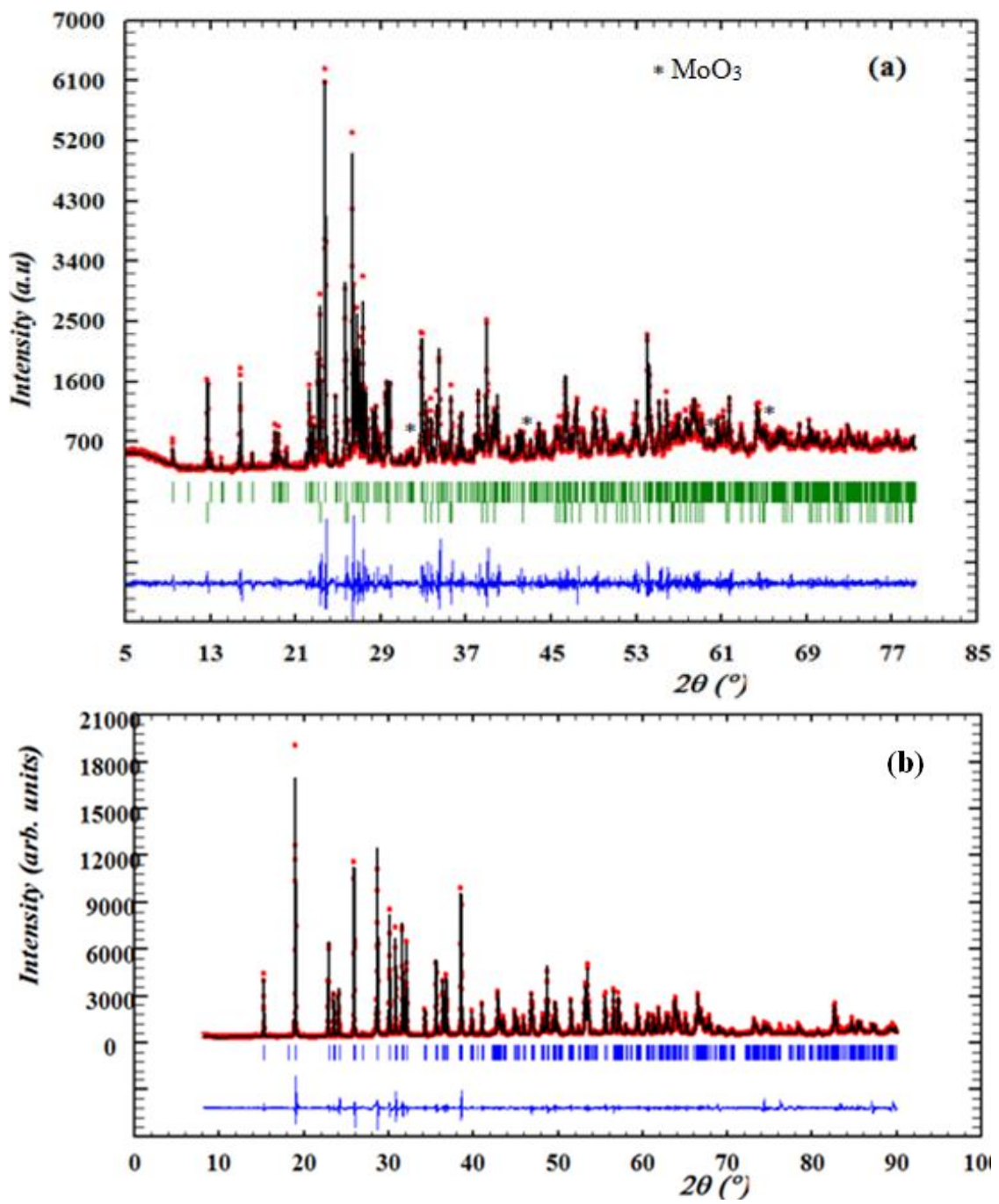


Figure. 1 : X-ray diffraction patterns and Rietveld refinement of α -CuMoO₄ (a) and CuWO₄ (b) samples recorded at room temperature.

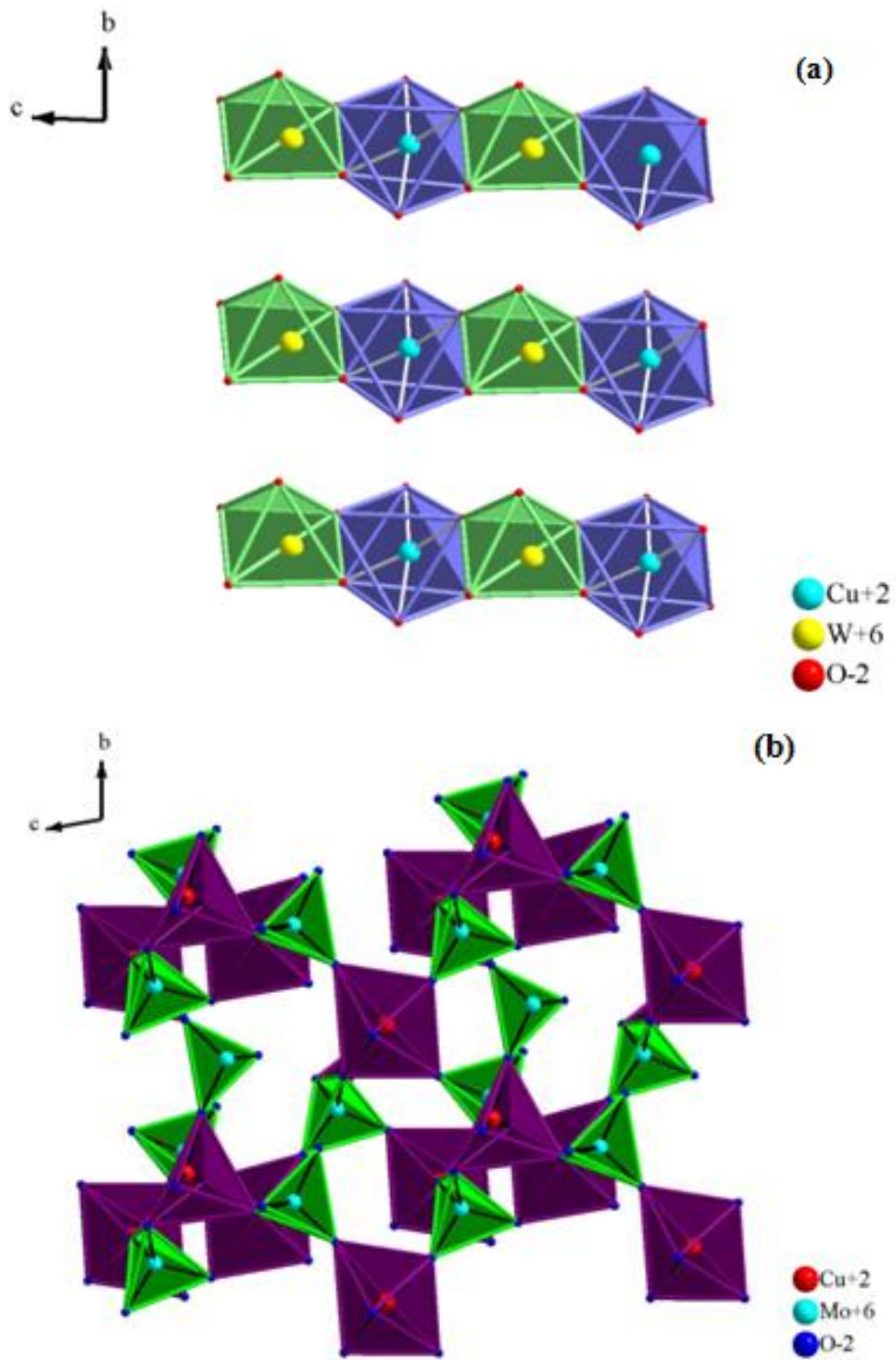


Figure. 2 : The crystal structure of CuWO_4 (a) and $\alpha\text{-CuMoO}_4$ (b) along a axis.

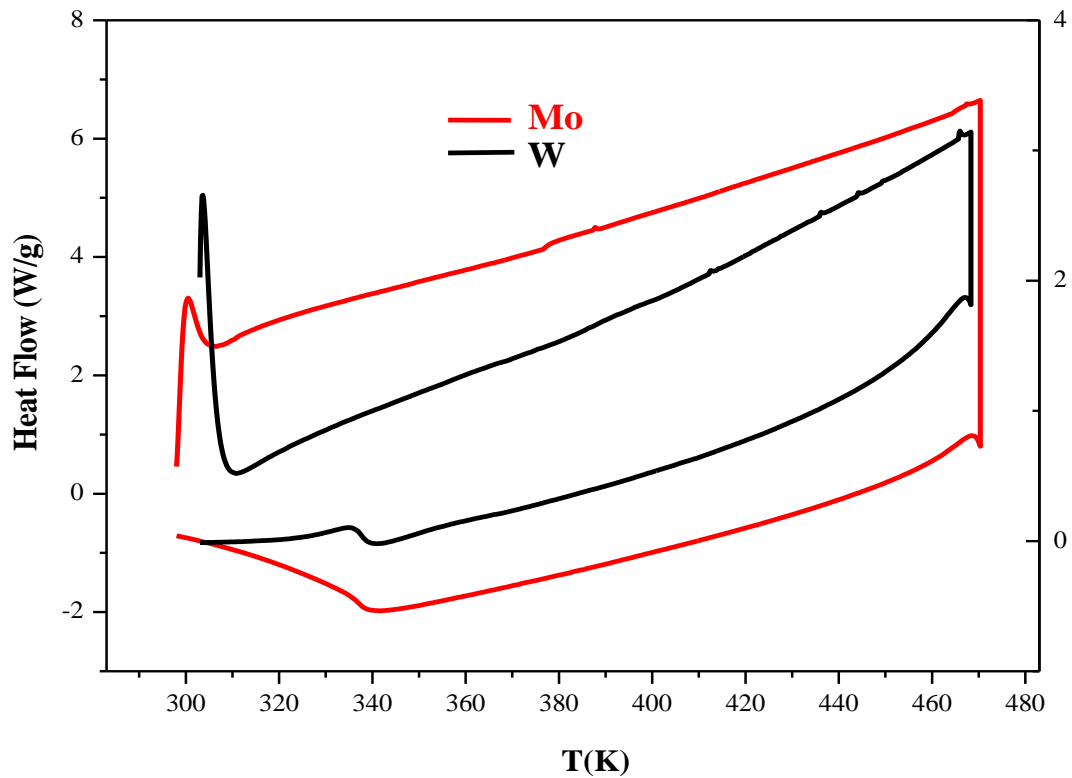


Figure. 3: DSC thermograms of α -CuMoO₄ and CuWO₄ compounds.

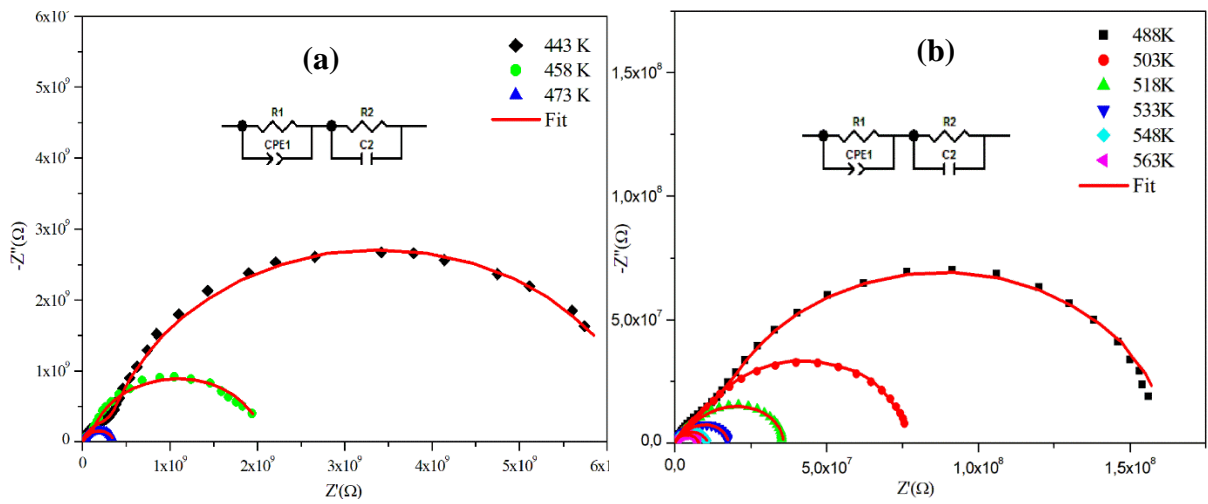


Figure. 4: Complex impedance spectra in the Nyquist plane with electrical equivalent circuit (inset), accompanied by theoretical data (Solid line) for α -CuMoO₄.

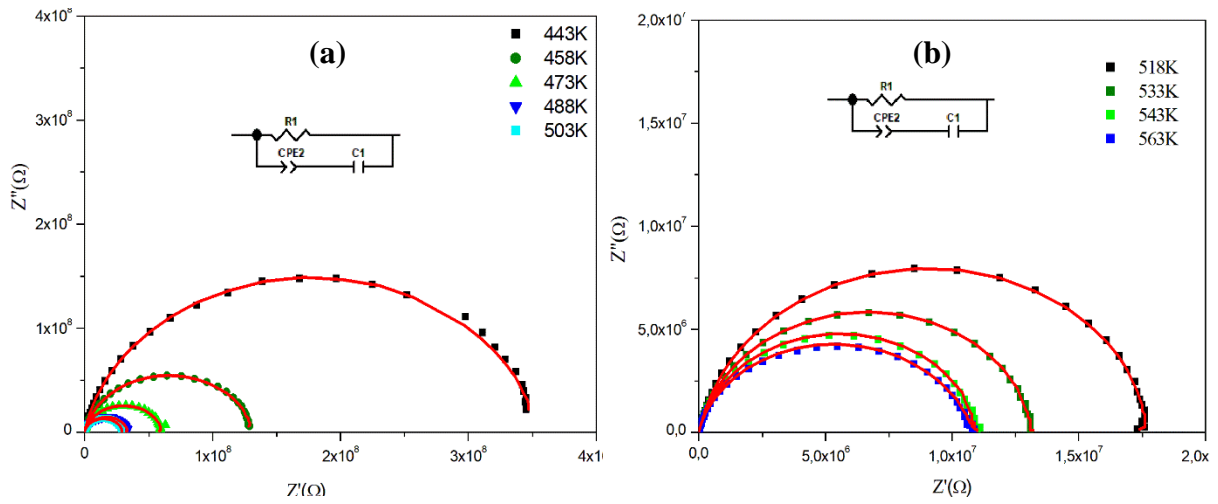


Figure. 5: Nyquist diagram spectra as a function of temperature and electrical equivalent circuit (**inset**) of the CuWO_4 compound.

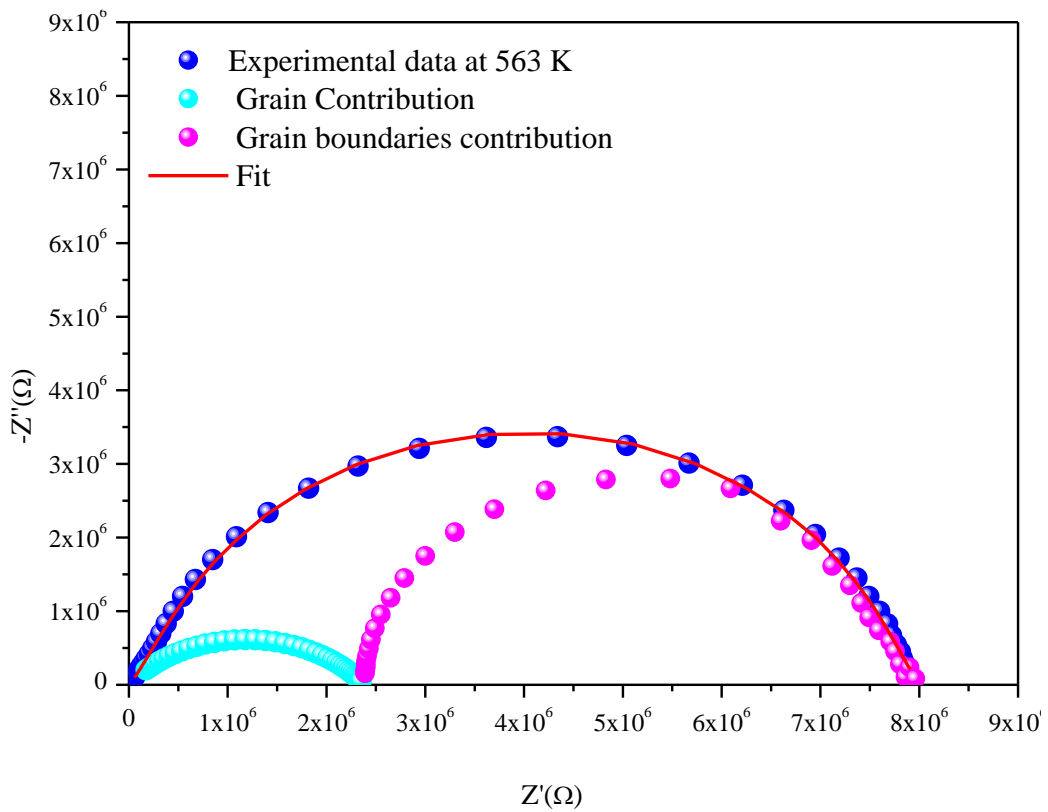


Figure. 6: Deconvolution of the Nyquist curve recorded at $T = 563 \text{ K}$.

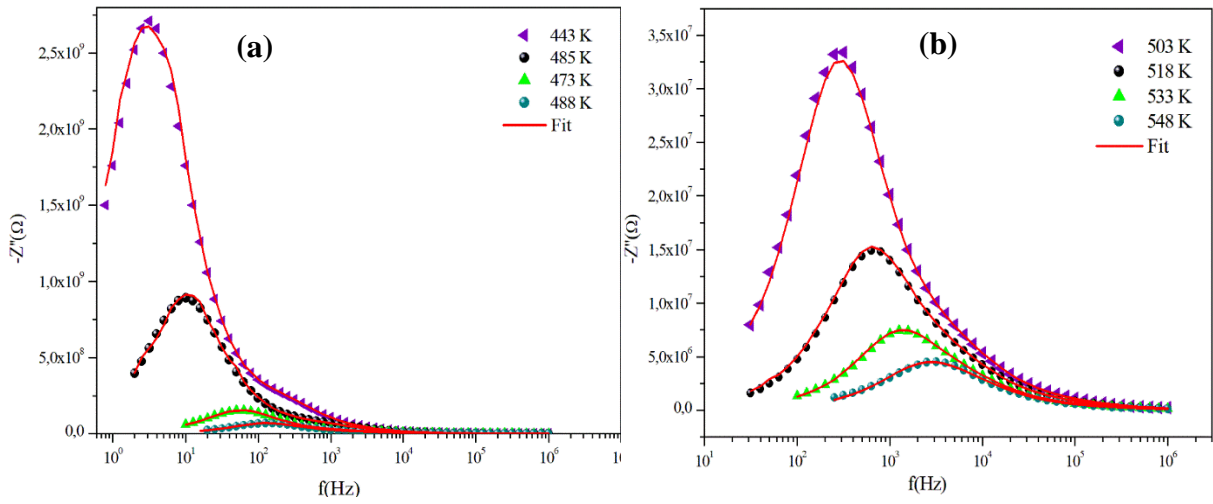


Figure 7: Variations of experimental and calculated imaginary parts of impedance ($-Z''$) as a function of frequency at some representative temperatures for α -CuMoO₄.

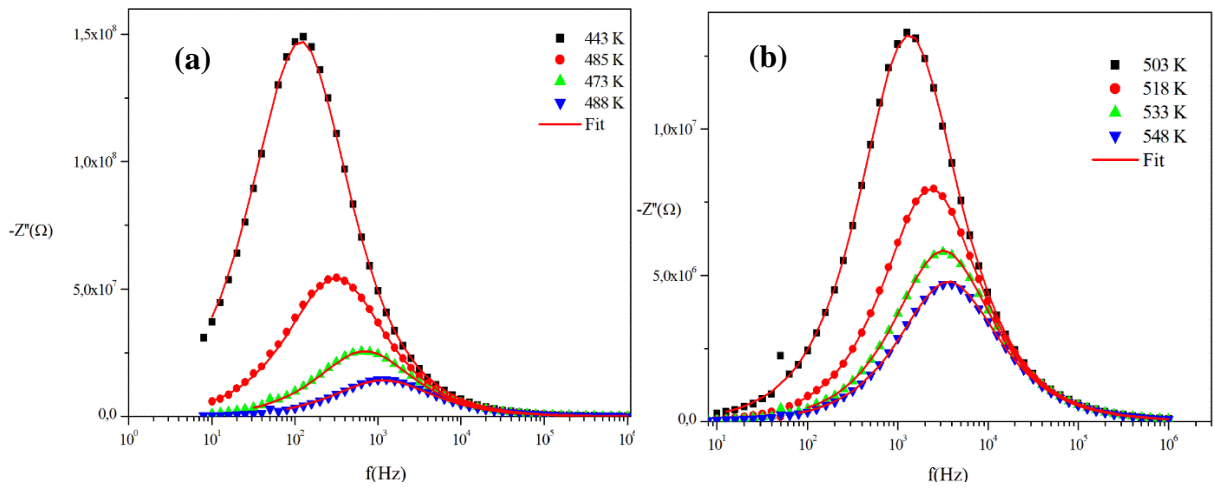


Figure 8: Variations of experimental and calculated imaginary parts of impedance ($-Z''$) as a function of frequency at several temperatures for CuWO₄ compound.

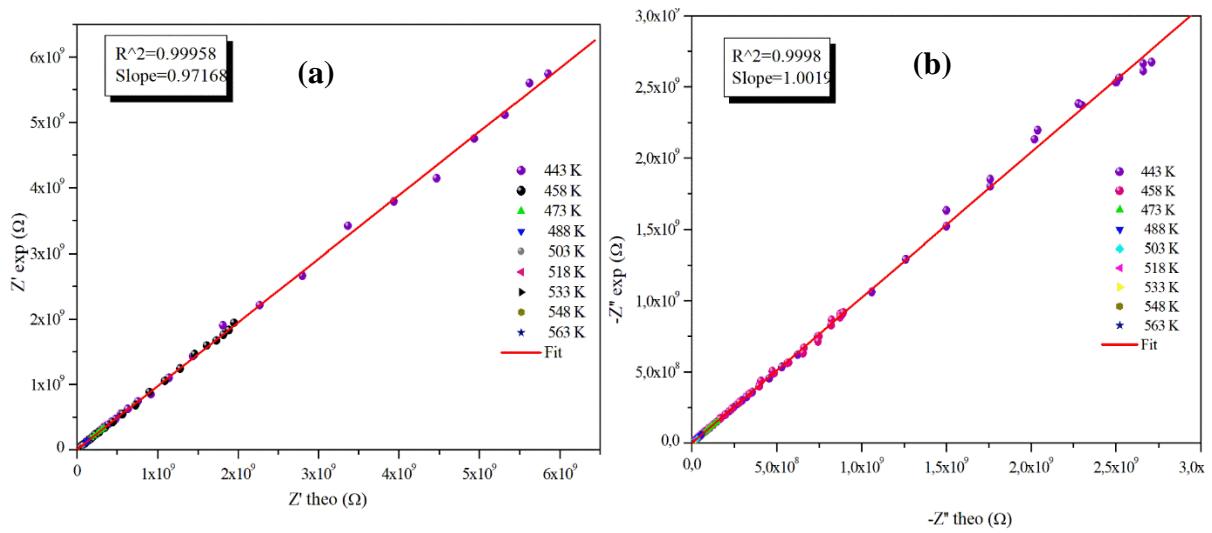


Figure. 9: Plots of measured values versus simulated values of the real and imaginary parts of the impedance for α -CuMoO₄ compound.

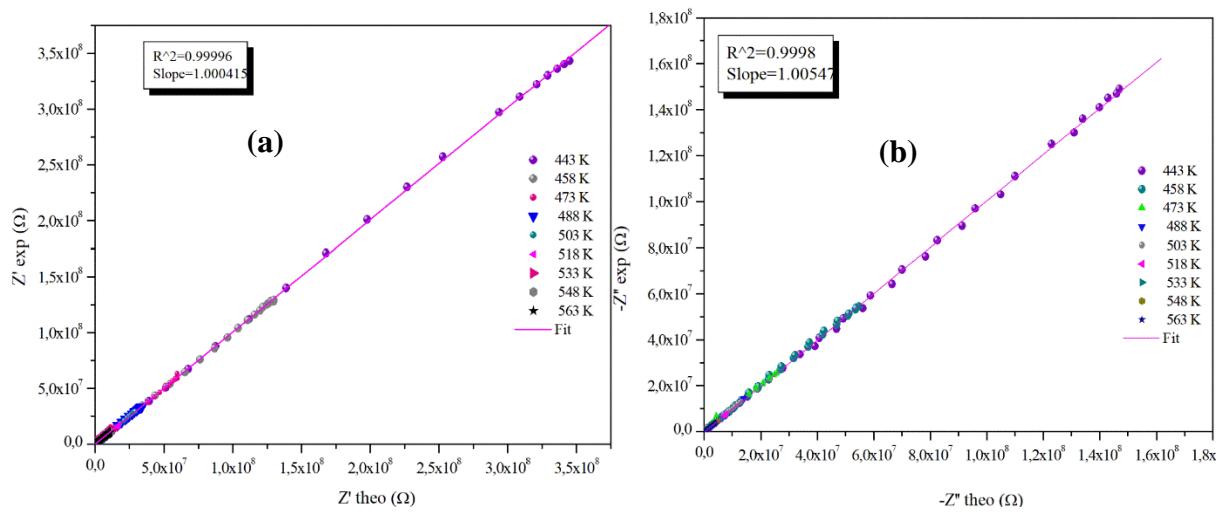


Figure. 10: Plots of measured values versus simulated values of the real and imaginary parts of the impedance for CuWO₄ compound.

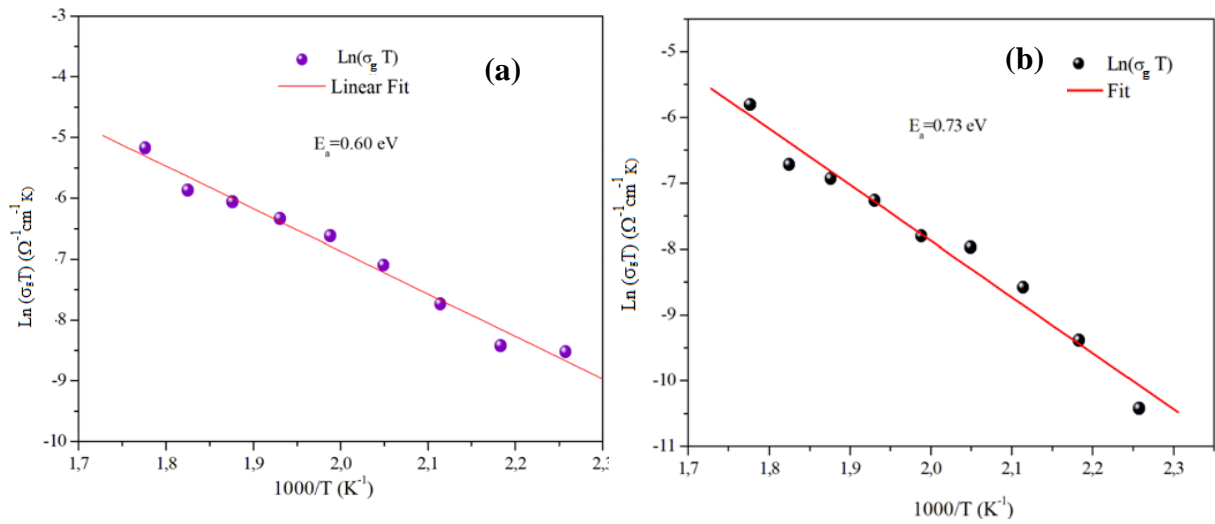


Figure. 11: Arrhenius plots for the bulk conductivity (a) of the $\alpha\text{-CuMoO}_4$ and (b) of CuWO_4 samples.

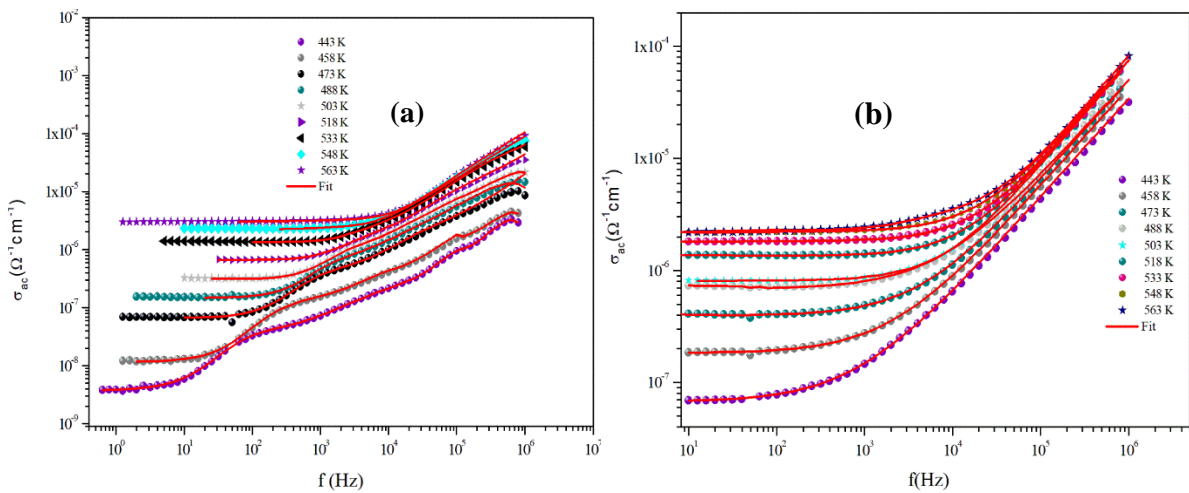


Figure. 12: Dependence of AC conductivity with the frequency at some temperature for $\alpha\text{-CuMoO}_4$ (a) and CuWO_4 (b).

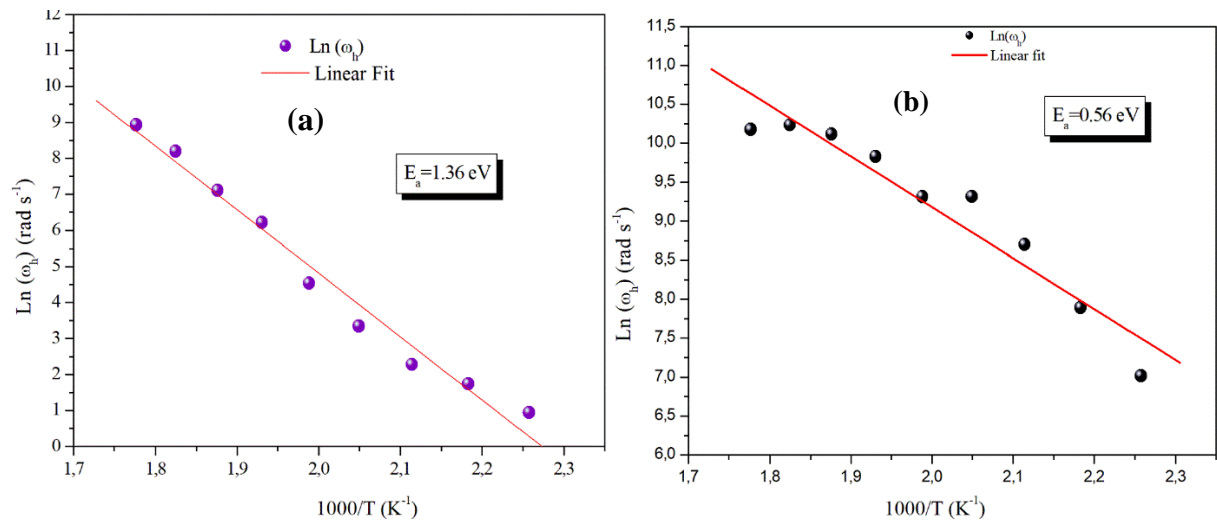


Figure. 13: Plot of hopping frequency ω_h against $1000/T$ for the compound $\alpha\text{-CuMoO}_4$ (a) and for CuWO_4 (b).

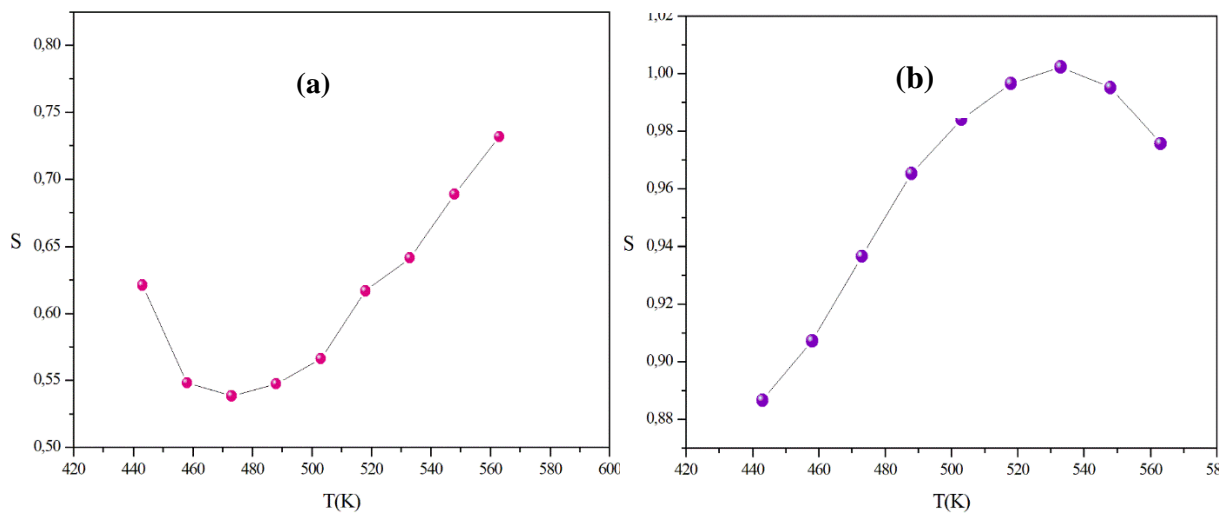


Figure. 14: The variation of the universal exponent s with temperature of the $\alpha\text{-CuMoO}_4$ (a) and of CuWO_4 (b) samples.

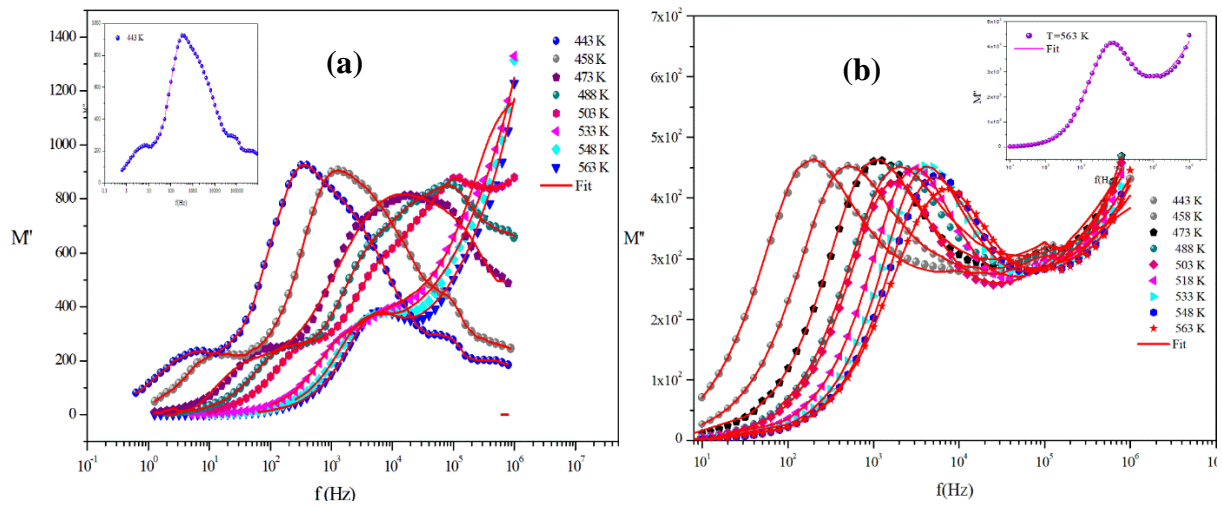


Figure. 15: The imaginary parts of the electric modulus as a function of frequency at several temperatures of α -CuMoO₄ (a) and CuWO₄ (b).

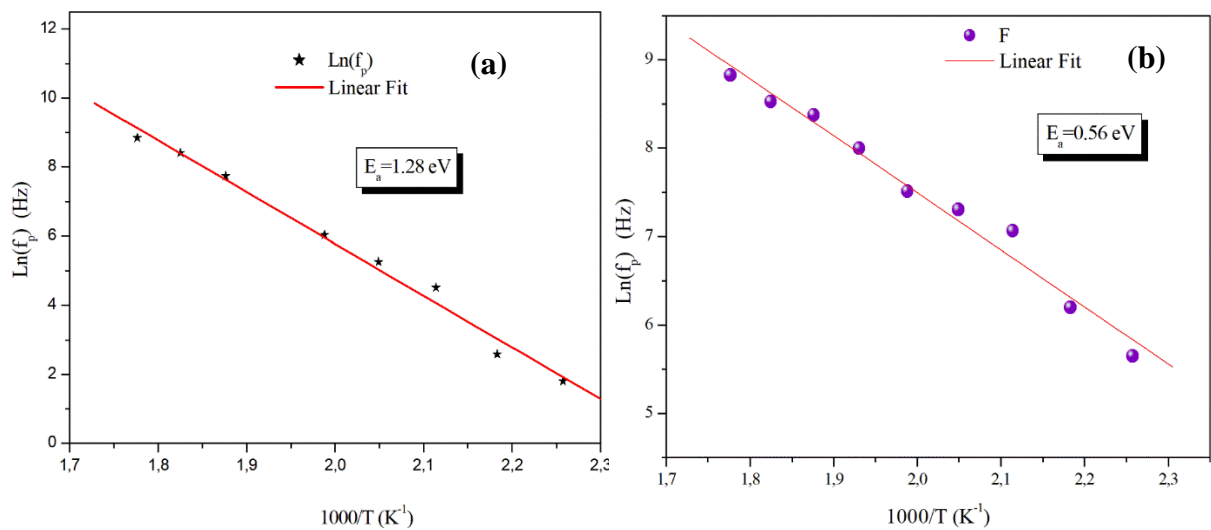


Figure. 16: Temperature dependence of the relaxation frequency f_p for the grains of α -CuMoO₄(a) and CuWO₄ (b).

Table 1: Conditions of synthesis of CuWO₄ and α -CuMoO₄.

Sample	Precursors	Synthesis	Color
CuWO ₄	CuO, WO ₃	773 K / 16 h, 1023 K/ 10 h	Light Yellow
α -CuMoO ₄	CuO, MoO ₃	773 K / 16 h, 923 K / 14 h	Green

Table 2: Crystallographic data of the structure refinement for CuWO₄ and α -CuMoO₄.

Formula	α -CuMoO ₄	CuWO ₄
Unit lattice parameters (Å)	a=6.789229(5)	a=4.7060 (4)
	b=8.37269 (3)	b=5.8415 (5)
	c=9.906073 (4)	c=4.8817 (4)
	$\alpha=96.892^\circ, \beta=107.009^\circ, \gamma=101.132^\circ$	$\alpha=91.881^\circ, \beta=92.497^\circ, \gamma=82.785^\circ$
Unit cell Volume (Å³)	V=568.70 (2)	V=136.89 (3)
Crystal system	Triclinic	Triclinic
Space group	$P\bar{1}$	$P\bar{1}$
R_{exp} (%)	10.66	06.2
R_p (%)	22.00	1.77
R_{wp} (%)	23.08	1.53
χ^2	4.02	3.1

Table 3: Activation energies and conductivities at 518 K for CuMO₄ (M=W, Mo) samples.

Formula	α -CuMoO ₄	CuWO ₄
E _{a,g} (eV)	0.60	0.73

W-O(Å)	-	1.79–2.20
Mo-O(Å)	1.74- 2.38	-
$\sigma_{503\text{ K}} (\Omega^{-1}\text{cm}^{-1})$	$2,6474310^{-6}$	$8,10010^{-7}$
A ($\Omega^{-1}\text{cm}^{-1}\text{ K}$)	2627.474	2262.84

Table 4: Electrical and dielectric parameters of the grains for CuWO_4 and $\alpha\text{-CuMoO}_4$ compounds.

Sample	$\text{Ln}(\sigma_g T)$	$\text{Ln}(f_p)$
CuWO_4	$E_a=0.73\text{ eV}$	$E_a=0.56\text{ eV}$
$\alpha\text{-CuMoO}_4$	$E_a=0.60\text{ eV}$	$E_a=1.28\text{ eV}$